A Letters Journal Exploring the Frontiers of Physics

December 2019

EPL, **128** (2019) 54006
doi: 10.1209/0295-5075/128/54006

www.epljournal.org

High-order harmonic generation from periodic potentials with different initial states

X. F. Pan, B. Li, T. Han, J. Zhang[a] and X. S. Liu[b]

Institute of Atomic and Molecular Physics, Jilin University - Changchun 130012, PRC

received 22 October 2019; accepted in final form 12 December 2019
published online 4 February 2020

PACS 42.50.Hz – Strong-field excitation of optical transitions in quantum systems; multiphoton processes and dynamic Stark shift
PACS 42.65.Ky – Frequency conversion; harmonic generation, including higher-order harmonic generation
PACS 78.47.-p – Spectroscopy of solid state dynamics

Abstract – In the single-active-electron model, we numerically solve the time-dependent Schrödinger equation to investigate the high-order harmonic generation (HHG) from solids. The results demonstrate that the intensity of the second plateau of the HHG with the initial multiphoton ionization channel is higher than that with the tunneling ionization channel, the cutoff energy of the harmonics with the initial multiphoton ionization channel is extended. We present a detailed analysis of the motion path of the electrons with the initial multiphoton ionization channel in the energy band structure, the results show that the electrons can be pumped directly to the conduction band at the multiphoton ionization channel. The time-dependent population imaging (TDPI) picture is used to further illustrate the excitation process of the electron, which is in agreement with the characteristics of the motion path of the electrons in the energy band structure.

Introduction. – High-order harmonic generation (HHG) has been studied widely in atomic and molecular systems theoretically or experimentally [1–4]. It is a nonlinear phenomenon and has also been used to generate attosecond laser pulses which opens a door to investigate the ultrafast processes [5–7]. Generally, the HHG can be described by the three-step model [8]. The electron can traverse the potential barrier and is ionized in the intense lasers field; then the electron is accelerated and obtains energy; finally, the electron can recombine with the parent ion when the orientation of the laser field is changed. However, the intensity of the HHG of the gas is low, which is due to the low gas density. The bulk crystal of the high intensity used to generate the high-order harmonic is efficient. Thus, the study of the HHG from bulk crystal of the high intensity has been widely concerned [9–11].

Comparing with the gases, the HHG from bulk crystal has many novel physical phenomena. For example, the cutoff energy of the bulk crystal HHG and the amplitude of the driving laser field are in linear relation, which depends on the crystallographic orientation [12]. The electron is restricted in the conduction band due to the periodic structure and it is not continually changed when it is ionized by the laser field [13,14]. For the process of the HHG in solids, previous work [15] has given a model of the step-by-step excitation: the electron in the position of the small band gap can be pumped to the different conductions. The ionized electron will recombine to the valence band with multi-channels to generate the high-order harmonics in one cycle, which is entirely different from the HHG mechanism from gases. Yu *et al.* [16] summarized the development of the primary numerical methods, such as the time-dependent Schrödinger equation (TDSE), semiconductor Bloch equations (SBE) and time-dependent density-functional theory (TDDFT).

In this paper, we investigate the HHG from solids by numerically solving the time-dependent Schrödinger equation (TDSE). We demonstrate that the intensity of the second plateau of the HHG is enhanced and the cutoff energy of the harmonics is extended with the initial multiphoton ionization channel. We show the time-dependent population imaging (TDPI) picture to illustrate the excitation process of the electron in different energy bands.

Theory and method. – In the single-active-electron model, the HHG from the solid can be investigated by numerically solving the one-dimensional time-dependent

[a]E-mail: jluzjun@jlu.edu.cn
[b]E-mail: liuxs@jlu.edu.cn

Schrödinger equation (TDSE). In the dipole approximation and length gauge, the TDSE reads (atomic units (a.u.) are used throughout, unless otherwise stated)

$$i\frac{\partial}{\partial t}\Psi(x,t) = [T + V(x) + xE(t)]\Psi(x,t), \tag{1}$$

where $T = \frac{\hat{p}^2}{2}$ is the kinetic energy, $\hat{p}$ is the momentum operator. We choose the Mathieu-type potential [17] as the periodic lattice potential. This model potential has been widely used to research the optical lattice and solid HHG [18–20]. The expression of the Mathieu-type potential is $V(x) = -V_0[1+\cos(2\pi x/a_0)]$, $V_0 = 0.37$ a.u. is the depth of the potential well of the solid. $a_0 = 8$ a.u. is the lattice constant.

The form of the electric field is given by

$$E(t) = E_0 \sin^2\left(\frac{\pi t}{6T_0}\right)\cos(\omega_0 t), \tag{2}$$

where E_0 is the amplitude of the electric field with the laser intensity $I_0 = 5.6 \times 10^{11}$ W/cm^2. T_0 is the optical cycle (o.c.), the duration time of the electric field is $6T_0$, $\omega_0 = 0.0153$ a.u. is the laser frequency, which corresponds to the laser wavelength $\lambda = 2963$ nm.

In order to obtain the energy-band structure and initial state with the field-free condition in the coordinate space, we numerically solve the eigenvalue equation by the finite-difference approximation,

$$\hat{H}_0\varphi_n(x) = E_n\varphi_n(x), \tag{3}$$

where φ_n and n are the eigenstate wave function and eigenstate number, which can be obtained by diagonalizing the field-free Hamiltonian [21]. The time-dependent wave functions can be obtained by the second-order splitting operator. We use the grid defined by -240 a.u. $< x < 240$ a.u. with the spatial step $\Delta x = 0.1$ a.u. and time step $\Delta t = 0.03$ a.u.. The number of the atoms in the linear chain is 60.

The harmonic spectrum can be obtained by calculating the Fourier transform

$$S(\omega) \propto \left|\int j(t)e^{i\omega t}\mathrm{d}t\right|^2, \tag{4}$$

where $j(t) = -\langle\Psi(t)|\hat{p}|\Psi(t)\rangle$ is the laser-induced current [22].

The TDPI picture can be obtained by calculating the instantaneous electron population on each eigenstate

$$|C_n(t)|^2 = |\langle\varphi_n|\Psi(t)\rangle|^2. \tag{5}$$

Results and discussion. – Figure 1 shows the energy band structure of the system in the reciprocal space. From fig. 1 we can see that there is one valence band and three conduction bands which are indicated as VB, CB1, CB2 and CB3 (the higher energy band has also been calculated, but it is not shown in fig. 1), respectively. From the energy band structure, we can illustrate the motion

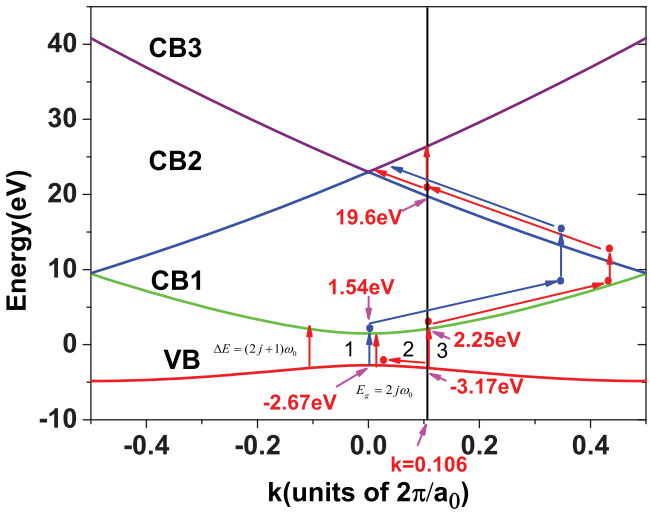

Fig. 1: The energy band structures in the reciprocal space. The blue and red arrow represent the motion path of the electron with the initial tunneling ionization channel at $k = 0$ and the initial multiphoton ionization channel at $|k| = 0.106$, respectively.

path of the electrons with the initial tunneling ionization channel and the initial multiphoton ionization channel. For the solid model, the tunneling ionization channel is located at $k = 0$ ($n = 120$), which is the position of the minimum energy interval (E_g) from the highest valence to the lowest conduction band. Recently, McDonald *et al.* [23] demonstrated that the multiphoton ionization channels ($2j+1, 2j+3, \ldots; j = 1, 2, 3, \ldots$) can be observed when the minimum energy interval is $E_g = 2j\omega_0$ (ω_0 is the driving laser frequency). In this paper, the minimum energy interval is $E_g = 0.153$ a.u. $= 10\omega_0$ ($j = 5$). Hence, the multiphoton ionization channels $(11, 13, 15, \ldots)$ can be observed. We only show the multiphoton ionization channel 13 ($\Delta E = 0.199$ a.u. $= 13\omega_0$, which is located at $|k| = 0.106$ ($n = 105$)) to illustrate the excitation process of the electrons (the excitation process of electrons with other multiphoton ionization channels is similar to the channel 13, thus it is not presented in this paper).

For the tunneling ionization channel, the electrons on the top of the VB can be pumped to the CB1 by tunneling ionization through path 1 as shown in fig. 1 [15]. The electrons on the CB1 can move to the edge of the first Brillouin zone driven by the laser field. Then the partial electrons can be pumped to the CB2 in the minimum band gap between CB1 and CB2. Similarly, the electrons on the CB2 can also be pumped to the CB3 at the minimum band gap between CB2 and CB3. The motion paths of the electron have been shown by the blue arrows in fig. 1.

For the multiphoton ionization channel, the electrons at $|k| = 0.106$ (the corresponding energy is -3.17 eV) in the VB will have two motion paths (path 2 and path 3 as shown in fig. 1) driven by the laser field. Path 2 shows that the electrons can move to the top of the VB. Then they are ionized by tunneling, which is similar to the path 1.

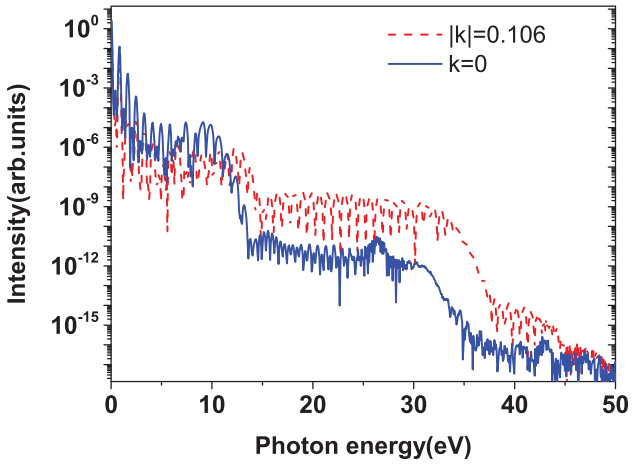

Fig. 2: Harmonic spectra from the periodic potential with the initial tunneling ionization channel ($k = 0$, blue solid line) and the initial multiphoton ionization channel ($|k| = 0.106$, red dashed line).

Another path (path 3) shows that the electrons can be pumped directly to the CB1 (the corresponding energy is 2.25 eV). Then the electrons in the CB1 can move to the edge of the Brillouin zone and will be pumped to the CB2. Moreover, the electrons in the CB2 at the energy of 19.6 eV ($|k| = 0.106$) have also two motion paths. The electrons in the CB2 at the energy of 19.6 eV can be pumped directly to the CB3, and partial electrons will move to the top of the CB2, and then can be pumped to the CB3. The motion path of the electron is shown by the red arrows in fig. 1. These reveal that the excitation process of the electron by choosing the multiphoton ionization channel is different from the tunneling ionization channel, which will be illustrated by the TDPI picture as shown in fig. 3.

We have demonstrated the HHG from the solid with the initial tunneling ionization channel ($k = 0$, blue solid line) and the initial multiphoton ionization channel ($|k| = 0.106$, red dashed line) as shown in fig. 2. The overall harmonic spectra have a distinct characteristic of the two-plateau structure. For the first plateau of the harmonic spectra, we can see that the intensity of the harmonic spectra with the initial tunneling ionization channel is higher than that with the initial multiphoton ionization channel. For the second plateau of the harmonic spectra, the intensity of the harmonic spectra with the initial multiphoton ionization channel is higher than that with the initial tunneling ionization channel, and the cutoff energy of the HHG is extended to the initial multiphoton ionization channel.

Generally, the primary contribution to generate the first plateau is the transitions from the first conduction band to the valence band, and the second plateau is originated by the transitions from the higher-lying conduction band [14]. The Keldysh parameter can be used to distinguish the ionization mechanisms in the atom and the solid system [24,25]. In the solids, the Keldysh parameter can be written as $\gamma = \frac{\omega_0\sqrt{mE_g}}{E_0}$ ($m = (1/m_e + 1/m_h)^{-1}$ is the reduced mass, m_e and m_h are the effective mass of the electrons and holes, respectively). When the amplitude of the laser field E_0 is weak or the laser frequency ω_0 is large, the Keldysh parameter $\gamma \gg 1$. The electron in the valence band can absorb multiple photons and pump to the conduction band. The multiphoton ionization is dominated in the ionization process. On the contrary, when the amplitude of the laser field E_0 is strong or the laser frequency ω_0 is small, the Keldysh parameter $\gamma \ll 1$. The electron in the valence band can pump directly to the conduction band. The tunneling ionization is dominated in the ionization process. When the Keldysh parameter $\gamma \sim 1$, both the multiphoton ionization and tunneling ionization can take place, which is a nonadiabatic process. In this paper, the amplitude of the electric field is set as $E_0 = 0.004$ a.u. ($I_0 = 5.6 \times 10^{11}$ W/cm^2). The Keldysh parameter is $\gamma = 0.525$, which indicates that the tunneling ionization is dominant [24]. The probability of the transition from the first conduction band to the valence band is increased with the initial tunneling ionization channel, which illustrates that the intensity of the harmonic spectra with the initial tunneling ionization channel is much higher than that with the multiphoton ionization channel in the first plateau of the harmonic spectra. Moreover, we can see that the electron excited to CB1 by multiphoton ionization can easily reach to the top of the CB2 as shown in fig. 1, which will have larger transition probabilities to the higher energy band. Thus, the intensity of the second plateau of the harmonic spectra with the initial multiphoton ionization channel is higher than that with the initial tunneling ionization channel.

In order to further investigate the physical mechanisms behind these phenomena, we demonstrate the TDPI picture with the initial tunneling ionization channel (fig. 3(a)) and the initial multiphoton ionization channel (fig. 3(b)), respectively. Four profiles of population oscillations in the energy band (VB, CB1, CB2 and CB3) are shown in fig. 3. We can see that the electrons generate strong oscillation and are restricted in every band, which is different from the continuous change of gases. Faisal *et al.* [26] presented a Floquet-Bloch theory to investigate the high-order harmonic generation with the periodic crystal structures. They found that the efficiency of the high-order harmonic generation for the semiconductor medium is higher than that for the insulator or the metal film. Moreover, the time-dependent Schrödinger equation can also be numerically solved by using the localized Wannier functions in one-dimensional conductor [27]. The cutoff of the solid HHG can be predicted when the electron is localized in one band and is defined by the maximum order or photon number: $N_m = eE_0a/\hbar\omega_0$, which is the ratio of the energy gain of an electron transfer between neighboring sites to the photon energy [27]. In this paper, we investigate the system of multiple energy bands, the strong oscillations are shown in the TDPI pictures. It is a highly delocalized process. The cutoff energy of the HHG spectrum can be predicted exactly from TDPI pictures [21]. For the initial

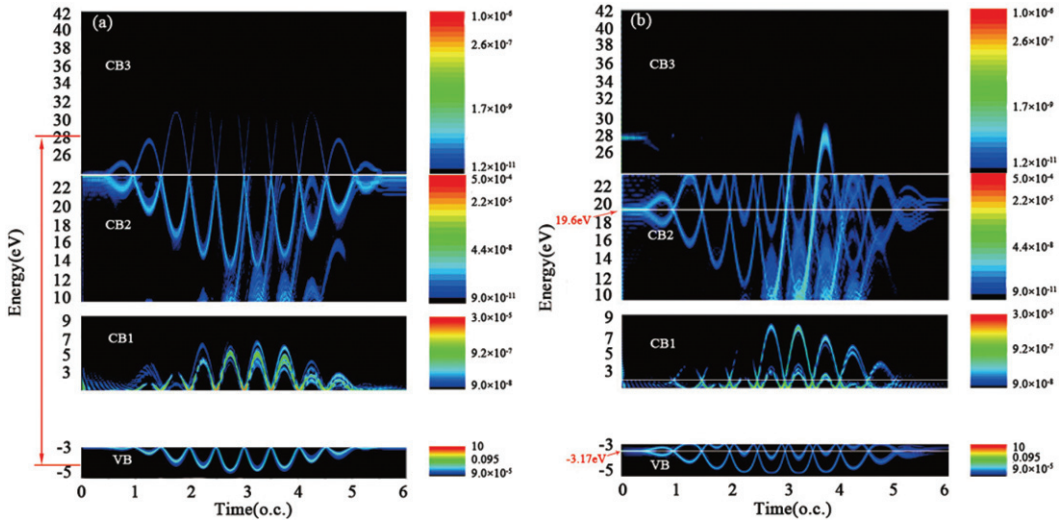

Fig. 3: Time-dependent population imaging (TDPI) picture with (a) the initial tunneling ionization channel and (b) the initial multiphoton ionization channel.

tunneling ionization channel, the energy range of the harmonic released by the electron transition between VB and CB3 is from −4 eV to 28 eV as shown by the red arrow in fig. 3(a). The cutoff energy of the HHG spectrum is the energy difference between VB and CB3 (32 eV), which is in agreement with the cutoff of the HHG spectra as shown by the blue solid line in fig. 2.

For the initial tunneling ionization channel, the electron can be ionized by tunneling at the position of the highest VB. Figure 3(a) shows that there are eight peaks in the VB and CB1. The intensity of the electron population in CB1 is higher than that of CB2 and CB3. Thus, the electron has a large population to transfer from CB1 to VB, and the intensity of the first plateau of the HHG is higher than that of the second plateau, which is in agreement with the characteristic of the HHG spectra as shown in fig. 2.

Figure 3(b) shows the TDPI picture with the initial multiphoton ionization channel. We can see that the energy of the electron in the VB at 0 o.c. is −3.17 eV, which is in agreement with the energy of the eigenstate at $|k| = 0.106$ as shown in fig. 1. In order to better analyze the TDPI picture with the initial multiphoton ionization channel, we have enlarged the TDPI picture of the VB and CB1 as shown in fig. 3(b), which is shown in fig. 4(a) and (b), respectively. In VB (CB1), we define the "large peaks" where the energy is lower (higher) than −3.91 eV (4.23 eV), which are shown by the red solid rectangular boxes, and the "small peaks" in which the energy is higher (lower) than −3.19 eV (4.23 eV) as shown by the white solid rectangular boxes. Figure 4 shows that there are eight large peaks and some small peaks in the VB and CB1.

We label with points A (and A′) the initial position of one of the large peaks and with points B (and B′) the initial position of one of the small peaks in the VB (and CB1) as shown in fig. 4(a) and (b), respectively. We can see that

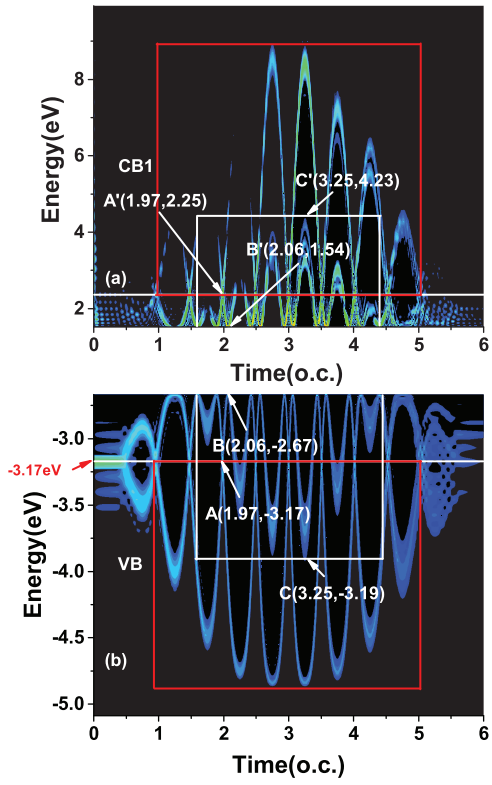

Fig. 4: The enlarged TDPI picture of the (a) CB1 and (b) VB as shown in fig. 3(b).

the energy of the position A in the VB and A′ in the CB1 at 1.97 o.c. are −3.17 eV and 2.25 eV, respectively. This means that the electrons can be pumped directly to the CB1 by the multiphoton ionization channel, which is in agreement with the path 3 as shown in fig. 1. These eight large peaks have the same initial energy, which can be observed with the evolution of the time-dependent population. Moreover, the energy of the position B in the VB

and the position B′ in the CB1 at 2.06 o.c. are −2.67 eV and 1.54 eV, respectively. The electron in the VB will move to the border of the Brillouin zone and then tunnel to the CB1, which is agreement with the path 2 as shown in fig. 1. These small peaks also have the same initial energy, they can be observed with the evolution of the time-dependent population. Comparing with the initial position of the larger peaks, the initial position of the small peaks has a delay time, which is due to the fact that the partial electrons need to move to the top of the VB, then they are ionized by tunneling, *i.e.*, the electrons need more time to be ionized.

For the CB2 and CB3, we can see that the electron population with the initial multiphoton ionization channel (fig. 3(b)) is higher than that with the initial tunneling ionization channel (fig. 3(a)). Thus, the electron will have a higher population to transfer from CB2 or CB3 to VB with the initial multiphoton ionization channel, and the harmonic intensity of the second plateau will be much higher, which is in agreement with the harmonic spectra as shown in fig. 2. Moreover, we can see that the electrons in the CB2 are reflected twice with the initial multiphoton ionization channel. On the one hand, the electrons reach to the edge of the Brillouin zone, partial electrons can be reflected in the CB2 and other electrons can be pumped to the CB3. On the other hand, the electrons generate the second reflection at the energy 19.6 eV, which corresponds to the energy of the eigenstate at $|k| = 0.106$ in CB2 as shown in fig. 1 (pink arrow), *i.e.*, the phenomenon is similar to that of the VB. This means that the electrons in the CB2 at the energy of 19.6 eV also have two motion paths. Partial electrons can be pumped directly to the CB3 at the energy 19.6 eV, and other electrons will move to the top of the CB2, and then they will be pumped to the CB3, which is in agreement with the motion path of the electron indicated by the red arrows in fig. 1.

Conclusions. – In summary, we investigated the HHG from periodic potentials with the initial tunneling ionization channel and the initial multiphoton ionization channel. Comparing with the initial tunneling ionization channel, the intensity of the second plateau of the harmonic spectra is enhanced and the cutoff energy is extended with the initial multiphoton ionization channel. It indicates that the electrons with the initial multiphoton ionization channel will be pumped directly to the conduction band which is demonstrated by the energy band structures. The TDPI picture is used to illustrate the motion path of the electrons, which is in agreement with the characteristics of the motion path of the electrons in the energy band structure.

* * *

This work is supported by National Natural Science Foundation of China (Grant Nos. 61575077, 11904122), Natural Science Foundation of Jilin Province of China (Grant No. 20180101225JC), China Postdoctoral Science Foundation (Grant Nos. 2018M641766 and 2019T120232); Graduate Innovation Fund of Jilin University (Grant No. 101832018C105).

REFERENCES

[1] Schafer K. J., Yang B., DiMauro L. F. and Kulander K. C., *Phys. Rev. Lett.*, **70** (1993) 1599.
[2] Kohler M. C., Klaiber M., Hatsagortsyan K. Z. and Keitel C. H., *EPL*, **94** (2011) 14002.
[3] Paul P. M., Toma E. S., Breger P., Mullot G., Augé F., Balcou P., Muller H. G. and Agostini P., *Science*, **292** (2001) 1689.
[4] Ge X. L., Du H., Guo J. and Liu X. S., *Opt. Express*, **23** (2015) 8837.
[5] Takahashi E. J., Lan P., Mücke O. D., Nabekawa Y. and Midorikawa K., *Nat. Commun.*, **4** (2013) 2691.
[6] Corkum P. B. and Krausz F., *Nat. Phys.*, **3** (2007) 381.
[7] Xia C. L., Zhang G. T., Wu J. and Liu X. S., *Phys. Rev. A*, **81** (2010) 043420.
[8] Corkum P. B., *Phys. Rev. Lett.*, **71** (1993) 1994.
[9] Yu C., Zhang X., Jiang S., Cao X., Yuan G., Wu T., Bai L. and Lu R., *Phys. Rev. A*, **94** (2016) 013846.
[10] Yu C., Jiang S., Wu T., Yuan G., Wang Z., Jin C. and Lu R., *Phys. Rev. B*, **98** (2018) 085439.
[11] Xia C. L., Li Q. Q., Cui H. F., Zhang C. P. and Miao X. Y., *EPL*, **125** (2019) 24004.
[12] Ghimire S., DiChiara A. D., Sistrunk E., Agostini P., DiMauro L. F. and Reis D. A., *Nature*, **7** (2011) 138.
[13] Liu L., Zhao J., Dong W., Liu J., Huang Y. and Zhao Z., *Phys. Rev. A*, **96** (2017) 053403.
[14] Wu M., Ghimire S., Reis D. A., Schafer K. J. and Gaarde M. B., *Phys. Rev. A*, **91** (2015) 043839.
[15] Jia G. R., Huang X. H. and Bian X. B., *Opt. Express*, **25** (2017) 23654.
[16] Yu C., Jiang S. and Lu R., *Adv. Phys. X*, **4** (2018) 1562982.
[17] Slater J. C., *Phys. Rev.*, **87** (1952) 807.
[18] Breid B. M., Witthaut D. and Korsch H. J., *New J. Phys.*, **8** (2006) 110.
[19] Chang R., Potnis S., Ramos R., Zhang C., Hallaji M., Hayat A., Gomez F. D., Sipe J. E. and Steinberg A. M., *Phys. Rev. Lett.*, **112** (2014) 170404.
[20] Pan X. F., Han T., Xia C. L., Xu T. T., Zhang J. and Liu X. S., *Laser Phys. Lett.*, **16** (2019) 115301.
[21] Liu X., Zhu X., Lan P., Zhang X., Wang D., Zhang Q. and Lu P., *Phys. Rev. A*, **95** (2017) 063419.
[22] Guan Z., Zhou X. X. and Bian X. B., *Phys. Rev. A*, **93** (2016) 033852.
[23] McDonald C. R., Vampa G., Corkum P. B. and Brabec T., *Phys. Rev. Lett.*, **118** (2017) 173601.
[24] Wang H., Feng Y., Fu S., Li J., Zhang X. and Du H., *Phys. Rev. A*, **99** (2019) 023406.
[25] Korbman M., Kruchinin S. Y. and Yakovlev V. S., *New J. Phys.*, **15** (2013) 013006.
[26] Faisal F. H. M. and Kamiński J. Z., *Phys. Rev. A*, **56** (1997) 748.
[27] Pronin K. A., Bandrauk A. D. and Ovchinnikov A. A., *Phys. Rev. B*, **50** (1994) 3473.